Nanoscale

ROYAL SOCIETY OF CHEMISTRY

PAPER

View Article Online
View Journal

Check for updates

Cite this: DOI: 10.1039/d4nr02364a

Tuning of plasmonic surface lattice resonances: on the crucial impact of the excitation efficiency of grazing diffraction orders†

Lynda Dehbi,[a] Pandey Kartikey,[b] Macilia Braik,[a] Abderrahmane Belkhir,[a] Stéphanie Lau-Truong,[b] Sarra Gam-Derouich,[b] Alexandre Chevillot-Biraud,[b] Claire Mangeney,[c] Abdelaziz Mezeghrane,[a] Fadi Issam Baida[d] and Nordin Felidj *[b]

Metallic nanoparticles exhibit remarkable optical properties through localized surface plasmon (LSP) resonances. When arranged in arrays, nanoparticles form surface lattice resonances (SLRs) affected by inter-particle distance. SLRs can offer narrower bandwidths and stronger electric field enhancements than LSP modes, crucial for efficient optical device development. Among important aspects, grazing diffracted orders crucially impact SLR properties, facilitating long-range nanoparticle interactions. This study explores how these photonic modes propagating at the substrate surface influence SLRs, by using experimental and theoretical approaches, including Finite Difference Time Domain simulations on gold disk arrays. Results show SLR properties strongly rely on diffracted mode efficiency controlled by the grating constant along the incident polarization. Notably, large inter-particle spacing along the incident polarization can strongly reduce the SLR red-shift. Understanding and managing long-range interactions in engineered plasmonic structures are highlighted, providing insights for enhanced performance in advanced photonic and optoelectronic devices.

Received 20th June 2024,
Accepted 27th November 2024

DOI: 10.1039/d4nr02364a

rsc.li/nanoscale

Published on 29 November 2024. Downloaded by Universite Paris Cite on 12/16/2024 10:29:44 AM.

1 Introduction

Metallic nanoparticles (NPs) absorb and scatter light thanks to their capability to sustain localized surface plasmon (LSP) resonances.[1–3] These resonances correspond to the coherent oscillations of surface conduction electrons in response to the incident electric field of light, leading to the emergence of an enhanced optical near-field.[4–6] The increase of the local field strength originates from significant dipole moment at optical frequencies induced by the electron oscillation. The LSP frequency of a metallic nanoparticle is closely linked to the plasma frequency of the free electrons, a parameter determined by the particle's size and shape, as well as the permittivity of the metal and the surrounding medium.[7–9] When these nanoparticles are arranged in a periodic lattice, their plasmonic resonances can couple with each other, leading to the emergence of new resonant modes called surface lattice resonances (SLRs).[10–14] SLR occurs if the diffraction order results in a surface wave propagating in the plane of the grating, known as the Rayleigh anomaly (RA).[15,16] In other words, SLR originates from the coupling between localized surface plasmon modes and grazing diffraction modes. Their frequency is of influenced not only by the optical response of individual nanoparticles but also by the lattice parameters such as the inter-particle distance (grating constant) and the array configuration. They may be characterized by a narrow bandwidth implying a strong enhancement of the electric field in the vicinity of the particles.[17,18] In the far-field, this long-distance coupling is evidenced by a red-shift in the wavelength of SLR mode as the grating constant increases, reaching a maximum of spectral shift for grating constant close to the incident light wavelength. Collective effects in 2D periodic arrays of nanoparticles have been investigated in numerous studies for fundamental understanding of the SLR effect,[19,20] and more recently in order to improve optical responses that are often not possible with single particles, such as high quality factors.[21–23] Indeed, such long-range interactions are particularly interesting since it results in improved enhanced light–matter interaction, compared to non-coupled nanoparticles, including enhanced light absorption, scattering, and

[a]Université Mouloud Mammeri de Tizi-Ouzou, LPCQ, BP 17 RP, 15000 Tizi-Ouzou, Algeria
[b]Université de Paris, Laboratoire ITODYS, CNRS, F-75006 Paris, France. E-mail: nordin.felidj@univ-paris-diderot.fr
[c]Université Paris Cité, CNRS, Laboratoire de Chimie et de Biochimie Pharmacologiques et Toxicologiques, F-75006 Paris, France
[d]Université de Bourgogne Franche-Comté, FEMTO-ST, CNRS, 25030 Besançon Cedex, France

† Electronic supplementary information (ESI) available. See DOI: https://doi.org/10.1039/d4nr02364a

Published on 29 November 2024. Downloaded by Universite Paris Cite on 12/16/2024 10:29:44 AM.

confinement of electromagnetic fields within the structures array, with distinct applications including sensing,[24,25] enhanced spectroscopy,[26,27] and photonic devices.[28] However, no study has yet examined the impact of the efficiency of diffracted orders in the substrate plane that facilitate coupling between the particles at long distances. This aspect is of crucial importance since it opens up the route for improvements in the monitoring of the long-range interactions, in terms of the SLR wavelengths and quality factors. Therefore, this study addresses the following questions: is there a significant impact of the efficiency of diffracted orders in the plane of the substrate on the SLR properties? And as a possible consequence, can we monitor the SLR properties through the control of the photonic modes propagating in the plane of the substrate?

To raise these questions, we propose in this article, to study experimentally the SLR properties supported by regular arrays composed of rectangular cells of gold nanoparticles, elaborated by electron beam lithography[29] and theoretically through Finite Difference Time Domain (FDTD) simulations.[30,31] Indeed, considering such configuration, will allow us to analyze the efficiency of the diffracted modes by changing the grating contant according to the direction of the incident polarization, and see the impact on the SLR resonance along the perpendicular direction, as schematized in Fig. 1. In doing this, we will show for the first time that the grazing modes propagating perpendicularly to the incident light polarization, at normal incidence, are strongly affected by the grating constant according to the incident polarization using as model systems, dielectric NPs. As a strong consequence, it is shown no red-shift is observed for large inter-particle spacing according to the incident polarization. Understanding and harnessing diffraction efficiency offer opportunities for developing advanced photonic and optoelectronic devices based on SLR resonances, with enhanced performance and functionalities.

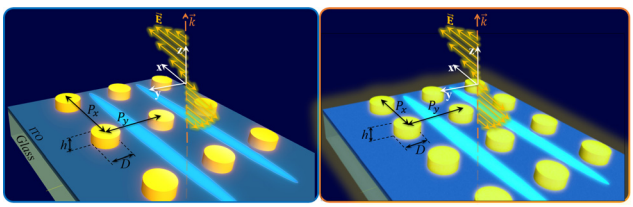


Fig. 1 Scheme of the rectangular arrays of disks: low diffraction efficiency (in blue box) *vs.* high diffraction efficiency (in red box) on the surface of rectangular arrays of gold disks featuring a diameter (D) and a fixed height (h). The grating constants in the x- and y-directions are denoted as P_x and P_y, respectively. The gold nano-disks are deposited onto a glass substrate coated with a thin layer of ITO. The polarization set along x-direction enables the excitation of Rayleigh anomalies propagating along the y-direction. The grating effect on SLRs is more efficient when the diffraction efficiency of the grazing orders is high, *i.e.* more energy is channeled onto the surface, (obtained for small interparticle distances along the polarization direction).

2 Results and discussion

To date, many fundamental and applied studies have been investigated on surface lattice resonance (SLR) have, using square, hexagonal or rectangular arrays of nanoparticles.[11,14,32–36] Others have studied the impact on coupling to the Rayleigh anomaly by modifying the size of the nanoparticles, which can also alter the surface plasmon response.[37–41]

To achieve our goal, we consider rectangular arrays of gold nano-disks, and show that such configuration enables us to elucidate the pivotal role of diffracted modes in SLR properties. Although many papers have addressed the use of rectangular arrays made of disks or rods, non of them pointed out the crucial role of the excitation efficiency of grazing diffraction orders on the SLR properties.[11,14,32,33,35,36,42] The distinct rectangular arrays of gold nano-disks are fabricated *via* Electron Beam Lithography (EBL), featuring a diameter (D) of 150 nm and a fixed height (h) of 50 nm. The grating constants in the x- and y-directions are denoted as P_x and P_y, respectively. The gold nano-disks are deposited onto a glass substrate coated with a thin layer of Indium Tin Oxide (ITO) measuring 80 nm in thickness. The superstrate considered in the present studies is air. The structure is illuminated by a linearly polarized plane wave along the x-axis from the substrate side. This polarization direction enables the excitation of Rayleigh anomalies propagating along the y-direction. The transmitted signal is collected in the same direction in air, and it is processed to determine the extinction spectra. This extinction is evaluated as $\log_{10}(1/T_0)$, where T_0 is the specular transmission of the structure. The investigation of the excitation efficiency and its impact on the SLR properties is made possible by simply varying P_x, corresponding also the incident polarization, as depicted in Fig. 1.

To explore the influence of the grating constant aligned with the polarization direction of the incident light (*e.g.*, along the x-axis) on the position of the SLR, we initially examined two arrays, with identical nanoparticle (diameter D = 150 nm) and a fixed y-axis period (P_y = 450 nm), while possessing two distinct x-axis periods (P_x = 220 nm and P_x = 400 nm). The fixed value of P_y at 450 nm is chosen strategically to align the spectral position of the RAs (0, ±1) closer to that of the LSP resonance of the NPs, thereby entering the regime of long-range interaction (or grating effect). Indeed, the slight disparity between the LSPR and the Rayleigh anomalies (0, ±1) enhances the radiative coupling of LSP to grazing diffracted orders. The experimental and FDTD extinction spectra of the two arrays are recorded with a polarization along the x axis, and presented in Fig. 2. Thus, polarization along the x-axis induces a diffracted mode perpendicular to it, namely, along the y-axis. The spectra show that the RAs (0, ±1) interact with the LSPR of the NPs, giving rise to an SLR mode, as anticipated. However, the experimental spectra, in close agreement with FDTD simulations, evidence a higher red-shift in the position of the SLR for P_x = 220 nm, compared to that of P_x = 400 nm. This discrepancy is surprising given that the grating

This journal is © The Royal Society of Chemistry 2024

Published on 29 November 2024. Downloaded by Universite Paris Cite on 12/16/2024 10:29:44 AM.

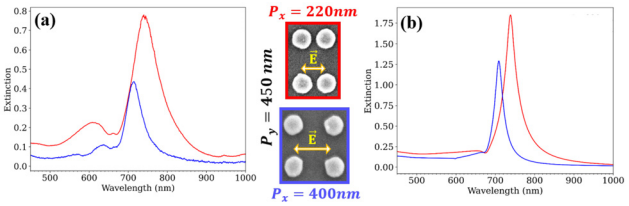


Fig. 2 SEM images of two rectangular arrays of gold disks with diameter D = 150 nm, height h = 50 nm and y-pitch P_y = 450 nm deposited on a glass substrate coated by a thin ITO layer (middle). The image in the red frame corresponds to P_x = 220 nm, while the one in the blue frame corresponds to P_x = 400 nm. The curves in (a) are the experimental and in (b) the calculated extinction spectra of the structures, recorded in air (superstrate) when the structure is illuminated at normal incidence from the glass substrate with an x-polarized plane wave. The red curves correspond to P_x = 220 nm while the blue ones correspond to P_x = 400 nm.

constant along the y-axis (P_y = 450 nm) remains identical for both arrays.

To confirm the observation, the extinction spectra by varying the grating constants along y-direction were recorded for distinct values of P_x with a polarization along the x-direction, varying from 220 nm to 600 nm: (a and a′) P_x = 220 nm; (b and b′) P_x = 300 nm; (c and c′) P_x = 400 nm and (d and d′) P_x = 600 nm, as shown in Fig. S1 and S2.† The experimental and calculated diagrams of dispersion were deduced (see Fig. 3). In all the presented cases, the FDTD calculations confirm and closely match the experimental results. If the alignment between simulation and experimental results is quite good for the dispersion diagram at P_x = 400 nm, with similar band widths in both cases at other pitches (*e.g.*, P_x = 300 nm), the experimental SLR bandwidths are broader than predicted by the FDTD method. This may be due to particle size polydispersity, despite precise electron beam lithography (EBL) calibration, and nanoscale surface roughness, which introduces damping effects on plasmon excitation.[43] Therefore, for identical values of P_y, the resonance wavelength—corresponding to the peak of extinction—is more red-shifted, as P_x decreases. Furthermore, the slope of the resonance band, in the extinction diagram, increases and is red-shifted when P_y increases (prior to reaching strong long-range interaction). This shift becomes particularly significant for small values of P_x. On the contrary, for very large P_x values (for instance P_x = 600 nm as in Fig. 3(d and d′)), the extinction band is almost flat indicating a very weak coupling regime between the RA and the LSP, whatever the P_y values. Same conclusions are observed by considering the similar lattice parameters, but for smaller NPs, with a diameter of D = 100 nm, as shown in the diagram of dispersion in Fig. S3 and S4.† Consequently, the grating constant in the direction of polarization exerts a substantial effect on the SLR spectral position even if the latter is linked to an anomaly propagating in the perpendicular direction (here y-direction). Consequently, the red-shift commonly observed with an increase in the grating constant P_y is influenced by the values of P_x when the incident polarization is along the x direction, as illustrated in Fig. S5.† This figure presents the spectral range of the red-shift in the SLR when varying the grating constant P_y for different P_x values. It demonstrates that as P_x increases, the magnitude of the SLR red-shift decreases with variations in P_y.

Note that the values of the gaps separating the nanoparticles in the x-direction considered in this work are large enough to inhibit any near-field coupling, in this direction,

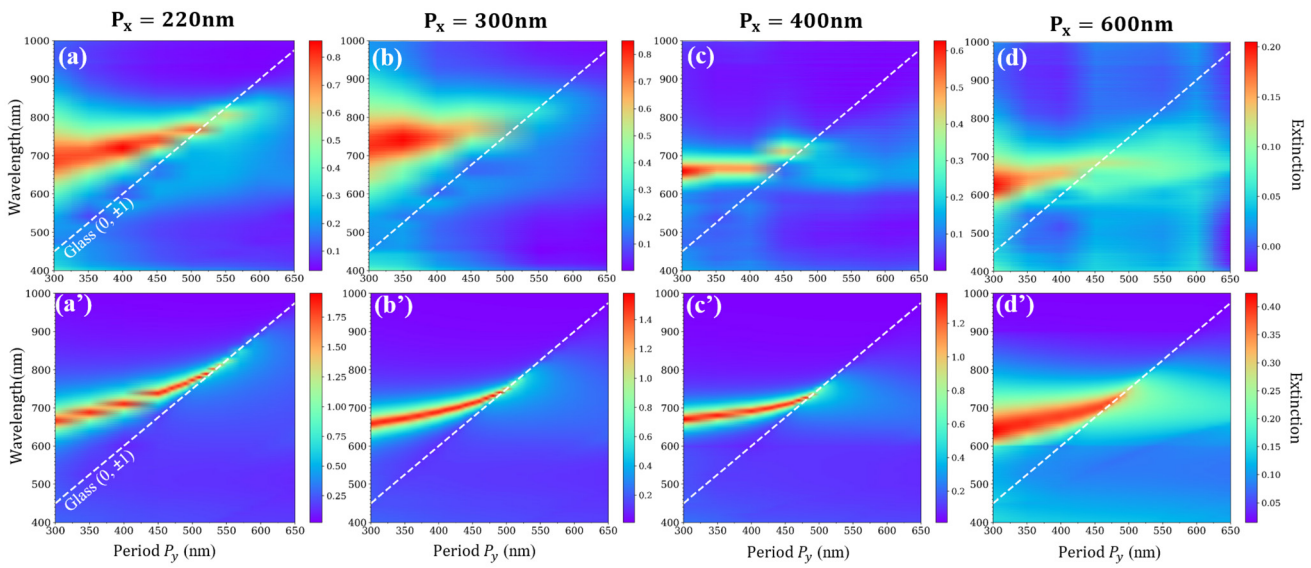


Fig. 3 (a–d) Experimental and (a′–d′) calculated diagrams of dispersion showing the SLR wavelengths *versus* P_y of the rectangular arrays of gold disks (150 nm in diameter and 50 nm high), supported by a glass substrate, and for fixed P_x = 220 nm, 300 nm, 400 nm and 600 nm. The polarization direction of the normal incidence wave is along the x-axis. The Rayleigh anomaly position is displayed in a white line for the (0, ±1) orders in the substrate.

Published on 29 November 2024. Downloaded by Universite Paris Cite on 12/16/2024 10:29:44 AM.

due to the overlap of the energy lobes of the plasmon resonances of the adjacent particles. As shown in Fig. S6,† near-field coupling only has an effect when the distance between the particles is less than 40 nm and only becomes significant when the distance is less than 20 nm. For distances between 40 nm and 60 nm, the position of the resonance shows a plateau towards λ = 607 nm, corresponding to the spectral position of the LSP resonance of an isolated particle as shown in the scattering efficiency spectrum of the isolated particle (see Fig. S6†). This demonstrates the quasi-absence of near-field coupling by overlapping of the energy lobs for gaps around 50 nm and obviously beyond.

In order to elucidate the role of the periodicity in the direction of polarization (here x-direction), the only credible hypothesis is to attribute it to the excitation efficiency (amplitude of the associated electromagnetic field) of the surface wave that is the Rayleigh Anomaly that couples with the LSP giving rise to SLR. To verify this hypothesis, while avoiding absorption phenomena that could influence the amplitudes of the various diffracted modes, we propose to consider a purely dielectric structure. In fact, it is well-known that dielectric nanoparticle arrays could support SLRs resulting from the coupling between Mie resonances of individual particles with the Rayleigh anomaly.[44–49] Nevertheless, for verification, we investigate a grating composed of a rectangular array of dielectric disks fabricated from a material with a high refractive index (n_D = 4),[49,50] each with a diameter of D = 120 nm and a thickness of h = 50 nm, deposited on a glass substrate. These specific parameters were selected to ensure that the scattering efficiency of an isolated disk (on a substrate) exhibits a Mie resonance within the visible spectrum, as demonstrated in Fig. 4a. This resonance is of the electric dipolar type, as can be seen from the distribution of the normalized electric field intensity shown in the inset of Fig. 4a. When transitioning to the periodic structure, we set the period along the y-direction to P_y = 300 nm (perpendicular to the incident polarization) to ensure the presence of resonant modes (RA) (0, ±1) near the isolated particle Mie resonance. Subsequently, these modes are coupled together to form a SLR. As expected, the extinction spectra of Fig. 4b, obtained for different values of the P_x period show the excitation of such SLRs. As in the case of gold nano-disks grating, these resonances are red-shifted compared to the case of the isolated particle, and this shift is more important when P_x decreases. Now, let's attempt to identify the underlying cause of this phenomenon based on our earlier assumption, which involves examining changes in the magnitude (efficiency) of the RA along the y-direction as the period along the x-direction (P_x) is varied. To this purpose, it is necessary to quantify this magnitude as a function of P_x. This requires a configuration where the RAs are far from any interaction with the eigenmodes of the scatterers. The all-dielectric grating offers us this possibility, since the Mie resonance is strongly influenced by the dielectric index of the nanoparticle.[50] Therefore, an optical refractive index of n_D = 2.2 for the disk shifts the Mie resonance at around 200 nm (see Fig. 5a), far from the (0, ±1), RA's wavelength which is 450 nm when P_y is fixed at 300 nm.

Fig. 5b shows the square modulus of the normalized electric field amplitude ($\tau_d = |E_d/E_{inc}|^2$) of the whole diffracted orders by the grating for different values of P_x. This quantity (τ_d) is calculated using relation: $\tau_d = 1 - T_0 - R_0$, where T_0 and R_0 are the specular transmission and reflection coefficients of the structure, respectively. This formula is justified by the inherent non-dissipative nature of our all-dielectric structure, meaning that no energy is lost by absorption. In the case where only the RAs (0, ±1) are excited (no more diffracted orders), this electric intensity corresponds to the one carried by these grazing modes.

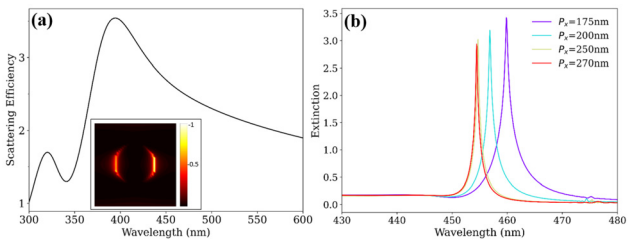


Fig. 4 Scattering efficiency of a single dielectric nano-disk of index n_D = 4 in (a), and extinction spectra of dielectric nano-disks' arrays of index n_D = 4 in (b). The inset in (a) corresponds to the electrical intensity distribution in the x–y plane, calculated just below the nano-disk, highlighting the electrically dipolar nature of the Mie resonance. The geometrical parameters of nano-disks are D = 120 nm as diameter and h = 50 nm as hight. The lattice parameter P_y is kept constant at 300 nm. Both the single nano-disk and the grating are supported by a glass substrate coated with a thin layer of ITO and surrounded by air as superstrate.

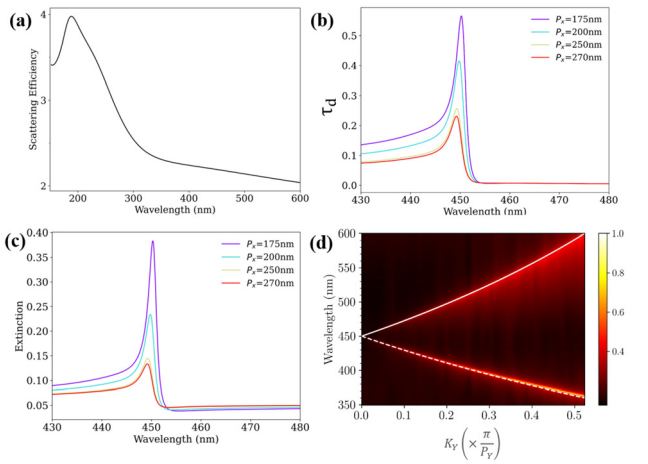


Fig. 5 (a) Scattering efficiency of an isolated disk of index n_D = 2.2. (b) Square modulus of the normalized electric field amplitude of the whole diffracted orders (diffraction efficiency) of dielectric disks' arrays of index n_D = 2.2 for different values of P_x and for fixed value of P_y = 300 nm. (c) Extinction spectra for the same arrays as considered in (b). (d) Corresponding photonic band structure, calculated by N-order FDTD, for one value of grating constant P_x = 250 nm. The solid and dashed white lines represent the RAs (0, −1) and (0, +1) respectively.

This journal is © The Royal Society of Chemistry 2024

Published on 29 November 2024. Downloaded by Universite Paris Cite on 12/16/2024 10:29:44 AM.

Fig. 5c shows the calculated extinction spectra corresponding to the gratings considered in Fig. 5b. As can be seen, the position of the extinction maxima coincides with the position of the grazing order diffraction efficiency maxima and does not change as a function of P_x. This is not the case when the index of the particle is high, here fixed at $n_D = 4$ (see Fig. 4b), where the position of the resonance in extinction is shifted to the red as P_x decreases (due to the interaction of the anomaly with the Mie resonance). This proves that for low nanoparticle index ($n_D = 2.2$) there is no interaction between the anomaly and the Mie resonance, which means that the missing energy in the far field (in the spectra in Fig. 5c) is indeed diffracted on the surface and quantified by the quantity τ_d.

The diffracted energy maximum, which is around $\lambda = 450$ nm whatever the value of P_x, corresponds to the fraction of energy carried by the diffracted order just before it changes from homogeneous (propagative) to evanescent at the wavelength of the Rayleigh anomaly. This wavelength value is obtained in the case of normal incidence from the formula bellow:[51]

$$\lambda_{RA}(l, m) = n\left[\frac{l^2}{{P_x}^2} + \frac{m^2}{{P_y}^2}\right]^{-1/2} \quad (1)$$

Here l and m are the diffracted wave orders along the x and y directions, respectively and n is the optical index of the substrate. Above λ_{RA} (0, ±1), τ_d decrease rapidly to zero for all values of P_x as seen in Fig. 5b. In this particular spectral range, only evanescent waves are excited as predicted by the formula (1), but without carrying any energy. From these results, we can conclude that this energy fraction associated with the RA (0, ±1) is greater when P_x is smaller, *i.e.* when the disks come closer together along the incident light polarization direction. The excitation efficiency of these grazing orders is higher for smaller P_x, which enhances their coupling with the Mie resonance (or localized surface plasmon resonance in the case of gold disks).

These observations are corroborated by a band structure calculation carried out on the same structure when the value of P_x is fixed at 250 nm (see Fig. 5d). As can be seen in this Figure, the two lower and upper branches are superimposed on the (0, +1) and (0, −1) anomalies (shown as dashed and solid white lines respectively). At the Γ point they tend to the same spectral position (450 nm) as that corresponding to the excitation of the two grazing orders (0, ±1) by a plane wave illuminating the structure at normal incidence (Fig. 5b). The spectral position of the maximum diffracted energy, independent of P_x and located at the same position as that of the anomalies, indicates the absence of any coupling with the Mie resonances of the nanoparticle (Fig. 5b). This is also confirmed by the absence of additional branches on the band diagram (Fig. 5d).

In a second step, we used the previous dielectric lattice to study the interaction between the Mie resonance and the Rayleigh anomalies by considering the nano-disk index $n_D = 4$. It is known that a sharp contrast index of the photonic crystal induces the removal of degeneracy at the Γ point, resulting in the appearance of a photonic band gap.

The band calculations carried out on this structure and shown in Fig. 6a and b indicate the presence of three branches in the case of $P_x = 175$ nm and four branches when $P_x = 270$ nm. In both cases, the lower and upper branches are tangent to the (0, +1) and (0, −1) anomalies, shown as dashed and solid white lines respectively. The central branch shown in the band diagram in Fig. 6a and the branch just below the upper branch in Fig. 6b correspond to the localized Mie mode supported by the nano-disks. The intensity of the additional branch that appears just above the lower branch (Fig. 6b), is relatively low, especially at low K_y values. Its position is around 405 nm, which corresponds to the position of the anomaly (±1, 0) in the substrate when $P_x = 270$ nm. It is independent of K_y in our case, which makes this branch horizontal. Note that this branch is not visible in Fig. 6a corresponding to $P_x = 175$ nm, because the position of the anomaly (±1, 0) is located at about 262.5 nm.

Near the Γ point, where the coupling is strong, the two band diagrams show only two branches. In this zone, the Mie mode couples with the anomalies, giving rise to two SLRs whose spectral positions are redshifted with respect to the anomaly wavelength. Similar results in relation to plasmonic SLRs were also reported by Tretnak *et al.*[52]

Outside the coherent coupling zone (*i.e.* far from the Γ point) the three branches coexist. As we move away from the Γ point, the Mie branch tends to flatten out (more rapidly for large P_x), while the other two merge completely with the lattice anomalies. It is important to note that the angular extension (along K_y) of the coherent coupling zone is larger the smaller P_x is. In addition, the redshift of the two SLRs near the Γ point is more pronounced when P_x is small. Fig. 6c shows the spectral energy density corresponding to a cross section at the Γ point of the band diagrams in Fig. 6a and b. As can be seen, the redshift is greater for smaller P_x. When compared with the far-field extinction spectra (see Fig. 4), it can be seen that the upper branch is a dark mode (absent in the extinction spectra), while the lower branch is a bright mode (present in the extinction spectra at the same wavelength).

In Fig. 7 we have superimposed the diffracted energies and the extinctions calculated in the far field in the cases corresponding to the absence ($n = 2.2$, Fig. 7a) and the presence ($n_D = 4$; Fig. 7b) of the coupling. As can be seen in Fig. 7a, the lack of energy transmitted in the far field, which results in a maximum extinction, is carried on the surface by the grazing

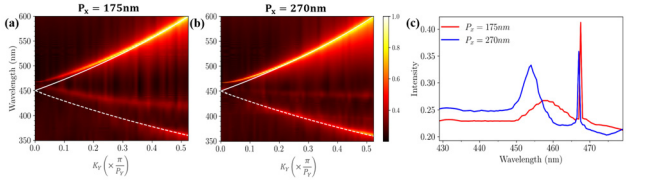


Fig. 6 Photonic band structure calculated by N-order FDTD for the dielectric structure of grating constants P_y fixed at 300 nm and P_x = 175 nm in (a) and P_x = 270 nm in (b). The solid and dashed white lines represent the RA(0, −1) and RA(0, +1), respectively. (c) Eigenmode calculation at Γ point ($k = 0$).

Published on 29 November 2024. Downloaded by Universite Paris Cite on 12/16/2024 10:29:44 AM.

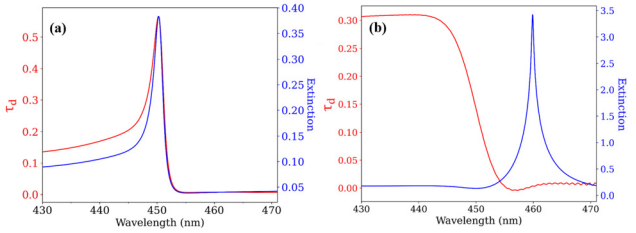


Fig. 7 Square modulus of the normalized electric field amplitude and extinction spectra of dielectric disks' arrays *vs.* light wave length when the refractive index of the disk is set equal to 2, 2 in (a) and to 4 in (b). The other parameters are diameter D = 120 nm, height h = 50 nm and periods P_y = 300 nm and P_x = 175 nm. The substrate is glass of refractive index n = 1.5.

orders (0, ±1), as confirmed by the superposition of the maxima of the extinction and diffracted energy spectra at wavelength 450 nm. For scatterers index of n_D = 4, the energy diffracted at the surface is almost zero at about 450 nm, as shown by the red curve in Fig. 7b. This is due to the radiative coupling of the grazing modes with the Mie resonance giving rise to a collective mode (SLR) (in blue in Fig. 7b). It can be concluded that for tuning the wavelengths of the grating resonances, the P_x parameter, which is often neglected when the gratings are illuminated by an x-polarised wave, is as important as the P_y parameter. The effect of P_x on the SLR positions is due to the in-plane diffraction efficiency of the (0, ±1) orders, which is more important when P_x is small. The spectral position of the SLR is therefore also tuned by the pitch along the propagation direction of the anomaly P_y (placing the anomalies close to the single particle resonance) and more importantly, tuned by the pitch along the polarisation direction P_x.

3 Conclusion

In this study, we experimentally investigated SLR properties in rectangular arrays of gold disk particles and complement our findings with Finite Difference Time Domain (FDTD) simulations. By varying the grating constant according to the incident polarization direction, we analyze the efficiency of diffracted modes and their impact on SLR resonance. Our results reveal a strong dependence of SLR properties on the grating constant and incident polarization along the same direction. These engineered devices can function as highly efficient optical sensors, utilizing precise control over SLRs in metallic nanoparticle arrays. By tuning the grating constant along the x axis, the excitation efficiency of grazing diffraction orders can be optimized, resulting in sensors with narrower bandwidths, stronger electric fields, and enhanced sensitivity, offering advanced and tunable nanoscale light manipulation. Overall, understanding and manipulating these resonances offer opportunities for developing advanced photonic and optoelectronic devices with enhanced performance and functionalities, underscoring the significance of our findings in advancing nanophotonic engineering.

4 Methods

4.1 Electron beam lithography

The arrays were made by EBL, and were observed and characterized by scanning electron microscopy (SEM) at 5 kV using Zeiss Supra 40 MEB-FEG as instrument without metallization.[29] In the EBL procedure, a 100 nm thick layer of PMMA (poly-methyl methacrylate) electron resist was spin coated on glass substrates covered with a 80 nm layer of transparent conducting indium tin oxide (ITO). In the exposure step, the desired structures were exposed to an electron beam which was scanned over the sample. Chemical development, thermal vacuum coating with gold and a lift-off procedure followed, which led to regular arrays of gold nano-disks of the desired cross-section and widths, 50 ± 5 nm height and 100 μm diameter on top of the ITO covered glass-substrate. This method allows us to control precisely the nanoparticle size, shape, and interparticle distance between nanoparticles. We have thus the ability to tune the plasmon resonance at any desired wavelength.[29,53]

4.2 UV-visible extinction spectroscopy

The LSP resonance of the samples were probed by far-field visible-NIR extinction micro-spectroscopy in the range of 500–900 nm, with an irradiation by a halogen lamp from the glass side at normal incidence. The spectrometer (LOT ORIEL model MS 260i) was coupled to an optical microscope (OLYMPUS BX 51) equipped with a 10× objective (numerical aperture N.A. 0.25). The investigated area is a circle of approximately 80 μm diameter, which is smaller than the structures array (100 × 100 μm^2).

4.3 Finite difference time domain (FDTD) calculations

Finite Difference Time Domain (FDTD) simulations were performed using a developed 3D-code for the optical proprieties investigation. The code takes into account the periodicity of the structure in x and y directions *via* Bloch's boundary conditions[31] and the upper and lower semi-infinite media in z direction through Perfectly Matched Layers (PML) conditions of Berenger.[54] The implemented Critical Points Drude model[55] deals with the dispersive nature of gold and ITO using different fitted parameters to match experimental values. The structure is illuminated, with a plane wave, at normal incidence from the substrate. In near field, the normalised electric field intensity is calculated in the vicinity of the gold disks, while the detector is placed far away from them for far field simulations of extinction spectra.

Data availability

Data for this article, including SEM images, UV-Vis measurements and raw data from FDTD calculations are available at figshare at **https://doi.org/10.6084/m9.figshare.26068189.v2**.

This journal is © The Royal Society of Chemistry 2024

Published on 29 November 2024. Downloaded by Universite Paris Cite on 12/16/2024 10:29:44 AM.

Conflicts of interest

There are no conflicts to declare.

Acknowledgements

The authors thank the thank PROFAS B+ programme of Algerian-French cooperation, Université Paris Cité, the Centre National de la Recherche Scientifique (CNRS), and ANR (Agence Nationale de la Recherche) and financial support of this work through Labex SEAM (Science and Engineering for Advanced Materials and devices), ANR-10-LABX-0096 and ANR-18-IDEX-0001.

References

1 K. M. Mayer and J. H. Hafner, *Chem. Rev.*, 2011, **111**, 3828–3857.
2 K. A. Willets and R. P. Van Duyne, *Annu. Rev. Phys. Chem.*, 2007, **58**, 267–297.
3 Y. Chen and H. Ming, *Photonic Sens.*, 2012, **2**, 37–49.
4 C. Girard and A. Dereux, *Rep. Prog. Phys.*, 1996, **59**, 657.
5 D. W. Pohl and D. Courjon, *Near field optics*, Springer Science & Business Media, 2012, vol. 242.
6 A. G. Nikitin, A. V. Kabashin and H. Dallaporta, *Opt. Express*, 2012, **20**, 27941–27952.
7 K. L. Kelly, E. Coronado, L. L. Zhao and G. C. Schatz, *The optical properties of metal nanoparticles: the influence of size, shape, and dielectric environment*, 2003.
8 T. R. Jensen, M. L. Duval, K. L. Kelly, A. A. Lazarides, G. C. Schatz and R. P. Van Duyne, *J. Phys. Chem. B*, 1999, **103**, 9846–9853.
9 M. M. Miller and A. A. Lazarides, *J. Phys. Chem. B*, 2005, **109**, 21556–21565.
10 N. Félidj, G. Laurent, J. Aubard, G. Lévi, A. Hohenau, J. Krenn and F. Aussenegg, *J. Chem. Phys.*, 2005, **123**, 221103-1–221103-5.
11 G. Vecchi, V. Giannini and J. G. Rivas, *Phys. Rev. B:Condens. Matter Mater. Phys.*, 2009, **80**, 201401.
12 V. Kravets, F. Schedin and A. Grigorenko, *Phys. Rev. Lett.*, 2008, **101**, 087403.
13 V. Giannini, G. Vecchi and J. G. Rivas, *Phys. Rev. Lett.*, 2010, **105**, 266801.
14 A. D. Humphrey and W. L. Barnes, *Phys. Rev. B:Condens. Matter Mater. Phys.*, 2014, **90**, 075404.
15 D. Maystre, *Plasmonics: from basics to advanced topics*, Springer, 2012, pp. 39–83.
16 A. Maradudin, I. Simonsen, J. Polanco and R. Fitzgerald, *J. Opt.*, 2016, **18**, 024004.
17 I. Ragheb, M. Braik, A. Mezeghrane, L. Boubekeur-Lecaque, A. Belkhir and N. Felidj, *J. Opt. Soc. Am. B*, 2019, **36**, E36–E41.
18 L. Zundel, A. May and A. Manjavacas, *ACS Photonics*, 2021, **8**, 360–368.
19 D. Dey and G. C. Schatz, *MRS Bull.*, 2024, 1–10.
20 V. G. Kravets, A. V. Kabashin, W. L. Barnes and A. N. Grigorenko, *Chem. Rev.*, 2018, **118**, 5912–5951.
21 K. Yang, Y. Chen, S. Yan and W. Yang, *Heliyon*, 2023, **9**, e16598-1–e16598-15.
22 B. Wang, P. Yu, W. Wang, X. Zhang, H.-C. Kuo, H. Xu and Z. M. Wang, *Adv. Opt. Mater.*, 2021, **9**, 2001520.
23 G. Li, X. Du, L. Xiong and X. Yang, *Adv. Opt. Mater.*, 2023, **11**, 2301205.
24 B. D. Thackray, V. G. Kravets, F. Schedin, G. Auton, P. A. Thomas and A. N. Grigorenko, *ACS Photonics*, 2014, **1**, 1116–1126.
25 Z. Li, C. S. Prasad, X. Wang, D. Zhang, R. Lach and G. V. Naik, *Nanophotonics*, 2023, **12**, 3721–3727.
26 M. Charconnet, C. Kuttner, J. Plou, J. L. García-Pomar, A. Mihi, L. M. Liz-Marzán and A. Seifert, *Small Methods*, 2021, **5**, 2100453.
27 I. Ragheb, M. Braïk, S. Lau-Truong, A. Belkhir, A. Rumyantseva, S. Kostcheev, P.-M. Adam, A. Chevillot-Biraud, G. Lévi, J. Aubard, L. Boubekeur-Lecaque and N. Félidj, *Nanomaterials*, 2020, **10**, 2201-1–2201-13.
28 G. Barbillon, *Int. J. Mol. Sci.*, 2022, **23**, 10592.
29 W. Gotschy, K. Vonmetz, A. Leitner and F. Aussenegg, *Appl. Phys. B*, 1996, **63**, 381–384.
30 D. M. Sullivan, *Electromagnetic simulation using the FDTD method*, John Wiley & Sons, 2013.
31 F. I. Baida and A. Belkhir, *Finite difference time domain method for grating structures*, 2012.
32 M. Kataja, T. Hakala, A. Julku, M. Huttunen, S. van Dijken and P. Törmä, *Nat. Commun.*, 2015, **6**, 7072.
33 R. Guo, T. K. Hakala and P. Törmä, *Phys. Rev. B*, 2017, **95**, 155423.
34 D. Khlopin, F. Laux, W. P. Wardley, J. Martin, G. A. Wurtz, J. Plain, N. Bonod, A. V. Zayats, W. Dickson and D. Gérard, *J. Opt. Soc. Am. B*, 2017, **34**, 691–700.
35 T.-L. Lim, Y. Vaddi, M. S. Bin-Alam, L. Cheng, R. Alaee, J. Upham, M. J. Huttunen, K. Dolgaleva, O. Reshef and R. W. Boyd, *ACS Nano*, 2022, **16**, 5696–5703.
36 M. S. Bin-Alam, O. Reshef, Y. Mamchur, M. Z. Alam, G. Carlow, J. Upham, B. T. Sullivan, J.-M. Ménard, M. J. Huttunen, R. W. Boyd, *et al.*, *Nat. Commun.*, 2021, **12**, 974.
37 S. R. K. Rodriguez, A. Abass, B. Maes, O. T. Janssen, G. Vecchi and J. G. Rivas, *Phys. Rev. X*, 2011, **1**, 021019.
38 A. Abass, S. R.-K. Rodriguez, J. Gómez Rivas and B. Maes, *ACS Photonics*, 2014, **1**, 61–68.
39 M. Sharma, L. Michaeli, D. B. Haim and T. Ellenbogen, *ACS Photonics*, 2022, **9**, 2702–2712.
40 Q. Le-Van, E. Zoethout, E.-J. Geluk, M. Ramezani, M. Berghuis and J. Gómez Rivas, *Adv. Opt. Mater.*, 2019, **7**, 1801451.
41 S. M. Sadeghi, W. J. Wing, R. R. Gutha, C. Sharp and A. Hatef, *J. Appl. Phys.*, 2017, **122**, 063102-1–063102-8.
42 I. Abid, W. Safar, M. Edely, N. Felidj, M. Lamy de la Chapelle and H. Shen, *J. Phys. Chem. C*, 2022, **126**, 8676–8683.

Published on 29 November 2024. Downloaded by Universite Paris Cite on 12/16/2024 10:29:44 AM.

43 I. Sow, J. Grand, G. Lévi, J. Aubard, N. Félidj, J.-C. Tinguely, A. Hohenau and J. Krenn, *J. Phys. Chem. C*, 2013, **117**, 25650–25658.
44 I. Allayarov, A. B. Evlyukhin, D. J. Roth, B. Chichkov, A. V. Zayats and A. Calá Lesina, *Adv. Photonics Res.*, 2024, **5**, 2300268.
45 G. W. Castellanos, P. Bai and J. Gómez Rivas, *J. Appl. Phys.*, 2019, **125**, 213105.
46 V. E. Babicheva and A. B. Evlyukhin, *J. Appl. Phys.*, 2021, **129**, 040902.
47 A. D. Utyushev, V. I. Zakomirnyi, A. E. Ershov, V. S. Gerasimov, S. V. Karpov and I. L. Rasskazov, *Photonics*, 2020, **7**, 24-1–24-11.
48 A. D. Utyushev, V. I. Zakomirnyi and I. L. Rasskazov, *Rev. Phys.*, 2021, **6**, 100051.
49 V. E. Babicheva and A. B. Evlyukhin, *Laser Photonics Rev.*, 2017, **11**, 1700132.
50 J. van de Groep and A. Polman, *Opt. Express*, 2013, **21**, 26285–26302.
51 A. Ndao, R. Salut, M. Suarez and F. I. Baida, *J. Opt.*, 2018, **20**, 045003.
52 V. Tretnak, U. Hohenester, J. R. Krenn and A. Hohenau, *J. Phys. Chem. C*, 2020, **124**, 2104–2112.
53 A. Hohenau, H. Ditlbacher, B. Lamprecht, J. R. Krenn, A. Leitner and F. R. Aussenegg, *Microelectron. Eng.*, 2006, **83**, 1464–1467.
54 J.-P. Berenger, *J. Comput. Phys.*, 1996, **127**, 363–379.
55 M. Hamidi, F. I. Baida, A. Belkhir and O. Lamrous, *J. Phys. D: Appl. Phys.*, 2011, **44**, 245101.

 This journal is © The Royal Society of Chemistry 2024